A Systematic Analysis of the Mechanical Exergy of an Airfoil by Using Potential Flow, Euler & RANS

M. AGUIRRE[a], S. DUPLAA[b], X. CARBONNEAU[c], A. TURNBULL[d]
ISAE-SUPAERO, Université de Toulouse, France

a. SAFRAN TECH miguel-angel.aguirre@safrangroup.com
b. ISAE-SUPAERO Sebastien.DUPLAA@isae-supaero.fr
c. ISAE-SUPAERO xavier.carbonneau@isae.fr
d. SAFRAN TECH andy.turnbull@safrangroup.com

Abstract:

The exergetic method is a new aerodynamic assessment tool mainly used for the analysis of future aircraft configurations. One of its major components is the mechanical exergy, representing the recoverable energy of an aerodynamic system: its analysis and comprehension is key for the optimization of an airframe (drag reduction). The mechanical exergy field is studied by following a systematic approach. Firstly, the potential flow around a cylinder is analyzed. Then, a Van Der Vooren transformation is used in order to obtain the potential flow around an airfoil. Afterwards, the compressibility effects are analyzed by using a 2D EULER solution. Finally, a 2D CFD RANS solution of the same airfoil is analyzed in order to add the viscous effects. This study shows that the only recoverable mechanical exergy is inside the viscous wake: the mechanical exergy available on the inviscid region is self-recovered. Moreover, this analysis led to an improvement of the formulation of the exergetic-based drag measurement method for wind tunnel applications.

Keywords: aerodynamics, exergy method, airfoil, potential flow, CFD

1   Nomenclature

$\dot{\mathcal{A}}$	=	total anergy outflow rate, W
a	=	speed of sound, m.s^{-1}
α	=	angle of attack, Degrees
C_D	=	drag coefficient
C_p	=	pressure coefficient ($= \frac{P_s - P_{s_0}}{\frac{1}{2}\rho_0 u_0{}^2}$)
c	=	airfoil chord, m
c_p, c_v	=	mass specific heat at constant pressure and at constant volume, J.kg^{-1}.K^{-1}
D	=	drag force, N
$\delta( )$	=	$( ) - ( )_0$, local variation of a parameter respect to the upstream value
$\dot{E}_u$	=	axial kinetic exergy outflow rate, W
$\dot{E}_v$	=	transverse kinetic exergy outflow rate, W
$\dot{E}_p$	=	boundary-pressure work rate, W

e	=	mass specific internal energy, J.kg^{-1} $(=c_v\, T_{s_0})$
$\dot{\varepsilon}_m$	=	mechanical exergy outflow rate across the survey plane, W
$\dot{\varepsilon}_{th}$	=	thermal exergy outflow rate, W
F	=	complex potential
Γ	=	circulation, m^2.s^{-1}
γ	=	ratio of specific heats
$\boldsymbol{i, j, k}$	=	unit vectors along the aerodynamic x-, y- and z-axes
K	=	Karman-Trefftz parameter
M	=	Mach number $(= u_0/a_0)$
μ	=	laminar dynamic viscosity, kg.m.s^{-1}
$\boldsymbol{n}$	=	$n_x\,\boldsymbol{i}$, $n_y\,\boldsymbol{j}$, $n_z\,\boldsymbol{k}$, local surface normal vector
P_s, P_t	=	static and total pressure, Pa
R	=	gas constant, J.kg^{-1}.K^{-1}
Re	=	Reynolds number $(= \rho_0\, u_0\, c\, / \mu_0)$
r	=	cylinder radius, m
ρ	=	air density, kg.m^{-3}
S	=	surface, m^2
s	=	mass specific entropy, J.kg^{-1}.K^{-1} $(=c_p\, ln(\,T_s) - R\, ln(\,P_s))$
T_s, T_t	=	static and total temperatures, K
t	=	thickness parameter
θ	=	trailing edge angle, rad
$\bar{\bar{\tau}}$	=	viscous stress tensor, Pa
V	=	u$\boldsymbol{i}$, v$\boldsymbol{j}$, w$\boldsymbol{k}$, local velocity vector, m.s^{-1}
W	=	complex velocity function
z	=	original complex plane variable $(=x+iy)$
Z	=	transformed complex plane variable $(=X+iY)$

Subscripts

0	=	Upstream values
b	=	body
c	=	center of the cylinder in the complex plane
ref	=	reference
out	=	outlet section
w	=	wake

2   Introduction

The exergy method was developed during the last century for the study of classical thermodynamic systems [1,2]. It is based on the second principle of thermodynamics and splits the total energy of a system into its recoverable part (the exergy) and its non-recoverable part (the anergy). The application of this theory for external aerodynamic analysis started about 15 years ago and it is still in use today [3-8]. In particular, it was Arntz [9] who developed the modern exergetic method, which is well suited for the analysis of CFD simulations. This method has proven to be very useful for the study of future aircraft configurations [10], but it is also very useful for the analysis of classical aerodynamic problems like airfoils and wings [11-13] because the exergy and the drag are related quantities. As a matter of fact, this method provides an alternative point of view and thus it can shed new light on the physical understanding of aerodynamics. Indeed, most of classical analyses are performed by using a mechanical approach (like near-field [14,15] and far-field methods [16-20]), but the exergy method is a pure thermodynamic approach. This is a clear opportunity to explore the classical aerodynamics in a very different way, leading to answers of practical problems that cannot be answered by the classical

methods. One example is the difficulty in obtaining a robust drag prediction formulation suited for wind tunnel measurements: the existing formulations [16-20] do not perform well when the survey plane is placed very close to the body. This is a real technical problem because the exergy method states that the exergy can be recovered (i.e., that drag can be reduced), and particularly the mechanical exergy is maximum in the vicinity of the body [9]. Thus, a robust formulation capable of providing an accurate prediction of the drag and the mechanical exergy near the body is needed: this is the main goal of the present article.

Some advances have been made before by the authors by splitting the drag coefficient curve of a classical airfoil into its exergy and anergy components [11]. Then, another step towards the objective was made for a classical airfoil [12], where it has been observed that only the exergy available inside the wake seemed to be recoverable. However, a more physical insight is required in order to validate that key observation: this is also another objective of this work.

In order to reach those objectives, a systematic approach is proposed. Firstly, the potential flow around a cylinder is analyzed. Then, a Van Der Vooren transformation is used in order to obtain the potential flow around an airfoil. Afterwards, the compressibility effects are analyzed by using a 2D EULER solution. Finally, a 2D CFD RANS solution of the same airfoil is analyzed in order to take into account the viscous effects. In each case, the drag and the exergy/anergy components are analyzed.

3   A review of the aerodynamic assessment methods

This section presents a brief recap of the drag and exergy methods used along this article.

3.1   System of reference

The reference system used hereafter is shown in Fig. 1. It has the x-axis aligned with the upstream flow direction and pointing rearwards, the y-axis points towards the right-hand side of the body and the z-axis points upwards. Moreover, when control volume formulations are used, it is assumed that the outlet section "S_{out}" of the control volume is a plane (called "survey plane") and it is placed normal to the x-axis. Also, the lateral surfaces are considered parallel to the upstream direction and far away from the body.
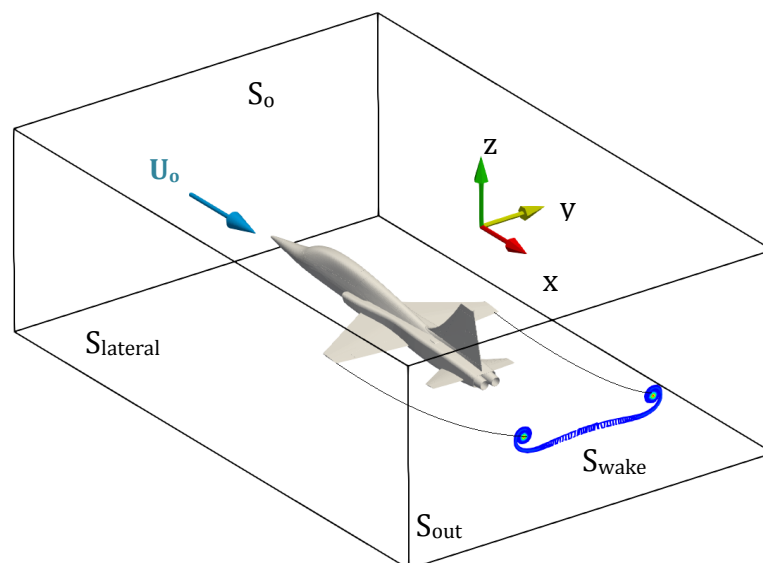

Fig. 1   Conventional reference frame.

3.2 Near-field method

The near field method is the classical approach used in order to obtain the total drag force "D" that's acting upon a body [14, 15]. It takes into account the pressure and viscous forces:

$$D = \int_{S_b} (P_s \overrightarrow{n_x} - \overline{\overline{\tau}} . \overrightarrow{n_x}) \, dS_b \tag{1}$$

3.3 Far-field method

The far-field method applies the momentum conservation equation to a control volume surrounding the body. Several variants of this method are available [16-20], allowing the extraction of the drag force by only analyzing the wake of a body. This paper only uses the most recent approach for the wind tunnel measurement of stationary flows [20]. It is based on the small perturbations method and the decomposition of the axial velocity deficit inside the wake. This leads to a profile drag equation:

$$D = \frac{\rho_0 \, u_0^2}{2} \int_{S_w} \left[-\frac{2}{\gamma \, M_0^2} \Delta P_t - \Delta T_t + \left(1 - \frac{M_0^2}{4} \right) \Delta T_t^2 - \Delta P_t \, \Delta T_t - (1 - M_0^2)(\Delta \bar{u}^2 + 2 \, \Delta u^* \, \Delta \bar{u}) \right] dS \tag{2}$$

Where:
$$\Delta Pt = \frac{P_t}{P_{t_0}} - 1 \tag{3}$$

$$\Delta Tt = \frac{T_t}{T_{t_0}} - 1 \tag{4}$$

$$\Delta u = \frac{u}{U_0} - 1 \tag{5}$$

$$\Delta u^* = \sqrt{1 - \frac{2}{(\gamma-1) \, M_0^2} \left(\left(\frac{P_s}{P_{s_0}} \right)^{\frac{(\gamma-1)}{\gamma}} - 1 \right) - \frac{v^2 + w^2}{U_0^2}} - 1 \tag{6}$$

$$\Delta \bar{u} = \Delta u - \Delta u^* \tag{7}$$

The "small perturbation" assumption considers that the variations of total pressure ΔP_t, total temperature ΔT_t and axial velocity Δu are small. Moreover, the velocity perturbation Δu is decomposed into a viscous contribution $\Delta \bar{u}$ (which is null outside the wake) and other component Δu^* that is related to the isentropic field.

3.4 Exergy method

The Arntz method [9] is well suited for CFD analysis and it provides an exergy-based drag force equation when an unpowered and adiabatic case is considered:

$$D * u_0 = \dot{\varepsilon}_m + \dot{\varepsilon}_{th} + \dot{\mathcal{A}} \tag{8}$$

Each term on the right-hand side represents an equation itself as indicated as follows:

$$\dot{\varepsilon}_m = \underbrace{\int_{S_{out}} \frac{1}{2} \rho \, \delta u^2 (\overrightarrow{V}.\vec{n}) dS}_{\dot{E}_u} + \underbrace{\int_{S_{out}} \frac{1}{2} \rho (v^2 + w^2)(\overrightarrow{V}.\vec{n}) dS}_{\dot{E}_v} + \underbrace{\int_{S_{out}} (P_s - P_{s_0})[(\overrightarrow{V} - \overrightarrow{V}_0).\vec{n}] dS}_{\dot{E}_p} \tag{9}$$

$$\dot{\varepsilon}_{th} = \int_{S_{out}} \rho \, \delta e \, (\vec{V}.\vec{n}) \, dS + \int_{S_{out}} P_{s_0}(\vec{V}.\vec{n}) \, dS - \underbrace{T_{s_0} \int_{S_{out}} \rho \, \delta s \, (\vec{V}.\vec{n}) \, dS}_{\dot{\mathcal{A}}} \tag{10}$$

The mechanical exergy outflow rate $\dot{\varepsilon}_m$ represents the amount of mechanical power that can be recovered by a so-called exergy recovery system (e.g., BLI - boundary layer ingestion). It is related to the axial and transverse velocity perturbations ($\dot{E}_u$ and $\dot{E}_v$ respectively) and the pressure perturbations ($\dot{E}_p$). The thermal exergy outflow rate $\dot{\varepsilon}_{th}$ represents the amount of thermal power that can be recovered. If the exergies are not valued (recovered) they will be gradually destroyed downstream, becoming a loss. In fact, the total anergy $\dot{\mathcal{A}}$ represents the total amount of energy that has been already lost by the system (quantified by the entropy increase). On the other hand, the drag, exergy and anergy values are non-dimensionalized by following the classical approach:

$$C_D = \frac{D}{\frac{1}{2}\rho_0 \, u_0^2 \, S_{ref}} \tag{11}$$

$$C_{D_\varepsilon} = \frac{\dot{\varepsilon}_m + \dot{\varepsilon}_{th} + \dot{\mathcal{A}}}{\frac{1}{2}\rho_0 \, u_0^3 \, S_{ref}} \tag{12}$$

$$C_{\dot{\varepsilon}} = \frac{\dot{\varepsilon}}{\frac{1}{2}\rho_0 \, u_0^3 \, S_{ref}} \tag{13}$$

$$C_{\dot{\mathcal{A}}} = \frac{\dot{\mathcal{A}}}{\frac{1}{2}\rho_0 \, u_0^3 \, S_{ref}} \tag{14}$$

The drag coefficient values are presented in drag counts, defined as one ten thousandth of C_D (1dc = 0.0001 C_D). The exergy-based drag coefficient is displayed in "power counts" (pc), defined as one tenth thousandth of "C_{D_ε}", i.e., 1pc = 0.0001 C_{D_ε} (The same applies for the exergy/anergy coefficients). Indeed, the exergy-based drag coefficient is equivalent to the force-based drag coefficient, thus, the power counts and drag counts units will be used interchangeably throughout this article.

NOTE 1: The terminology and notation of the exergetic method is not completely standardized yet [9]. In particular, "Anergy" is also called "exergy destruction" in the fluid dynamics domain [8].

NOTE 2: the Arntz formulation considers steady flow. Thus, for turbulent flows, the exergy components use time-averaged parameters. This is acceptable for the typical values of turbulence in aeronautical applications. However, the question is raised for cases of large-scale turbulence because the fluctuating velocity and pressure components must carry a significant amount of exergy. This will require an unsteady formulation (out of the scope of the present work).

3.5   Exergy-breakdown method

The Arntz method [9] is well adapted for CFD analysis because it requires an integration of data on the entire survey plane. However, it is not feasible in a wind tunnel environment, where data is obtained inside the wake only. Thus, a new exergy formulation adapted for wind tunnel testing was recently developed by the authors [21]. It is based on an improvement of the velocity decomposition proposed by Meheut [20] and requires extracting the isentropic velocity field V^* from the real flow field:

$$V^* = u_0 \sqrt{1 - \frac{2}{(\gamma-1)\,M_0{}^2}\left[\left(\frac{P_t}{P_{t_0}}\right)^{\frac{(\gamma-1)}{\gamma}} * \zeta - 1\right]} \tag{15}$$

With:
$$\zeta = 1 + \frac{\gamma-1}{2}M_0{}^2\left(1 - \frac{|\overline{V}|^2}{u_0{}^2}\frac{T_{t_0}}{T_t}\right) \tag{16}$$

The components of this isentropic velocity (also called "reversible") are then calculated from the real velocity vector components:

$$u^* = V^* \cos(\alpha)\cos(\beta) \tag{17}$$

$$v^* = V^* \cos(\alpha)\sin(\beta) \tag{18}$$

$$w^* = V^* \sin(\alpha) \tag{19}$$

With:
$$\alpha = arctg\left(\frac{w}{u}\right) \tag{20}$$

$$\beta = arctg\left(\frac{v}{u}\right) \tag{21}$$

Then, the isentropic components of the mechanical exergy, thermal exergy and exergy-based drag coefficient are calculated as follows:

$$\dot{\varepsilon}_m^* = \int_{S_{out}} \frac{1}{2}\rho(u^* - u_0)^2\, u^*dS + \int_{S_{out}} \frac{1}{2}\rho(v^{*2} + w^{*2})\, u^*dS + \int_{S_{out}} (P_s - P_{s_0})(u^* - u_0)dS \tag{22}$$

$$\dot{\varepsilon}_{th}^* = \int_{S_{out}} \rho\, \delta e\; u^*\, dS + \int_{S_{out}} P_{s_0}\, u^*\, dS - T_{s_0}\int_{S_{out}} \rho\, \delta s\; u^*\, dS \tag{23}$$

$$C_{D_\varepsilon}^* = \frac{\dot{\varepsilon}_m^* + \dot{\varepsilon}_{th}^*}{\frac{1}{2}\rho_0\, u_0{}^3\, S_{ref}} \tag{24}$$

And their viscous components (also called "irreversible" components) are given by:

$$\overline{\dot{\varepsilon}_m} = \dot{\varepsilon}_m - \dot{\varepsilon}_m^* \tag{25}$$

$$\overline{\dot{\varepsilon}_{th}} = \dot{\varepsilon}_{th} - \dot{\varepsilon}_{th}^* \tag{26}$$

$$\overline{C_{D_\varepsilon}} = C_{D_\varepsilon} - C_{D_\varepsilon}^* \tag{27}$$

By subtracting the isentropic component from the total field, only the viscous component remains and thus, it is only limited to the wake. Hence, a formulation suited for wind tunnel testing is obtained.

4 Potential flow equations

4.1 Flow around a cylinder

The potential flow around a cylinder with circulation can be obtained by adding several basic flows based on the superposition principle [22,23]. In order to simplify this task, a complex-variable approach is used. This treats the elemental flows as complex functions "F(z)" on the complex plane z=x+iy. These functions are called complex potentials and they are given by:

- Uniform flow:
$$F(z)_{uniform} = u_0 \, z \, e^{-i\alpha} \tag{28}$$

- Doublet:
$$F(z)_{doublet} = \frac{u_0 \, r \, 2 \, e^{-i\alpha}}{z - z_0} \tag{29}$$

- Vortex:
$$F(z)_{vortex} = \frac{-i \, \Gamma \, \ln(z - z_c)}{2\pi} \tag{30}$$

Then, the flow around a cylinder is obtained by summing-up these functions:

$$F(z)_{cylinder} = F(z)_{uniform} + F(z)_{doublet} + F(z)_{vortex} \tag{31}$$

Once the complex potential is stablished, its derivative is performed in order to obtain the complex velocity:

$$W(z) = \mathrm{d}F(z)/dz \tag{32}$$

For the elementary flows mentioned earlier, this becomes:

- Uniform flow:
$$W(z)_{uniform} = u_0 \, e^{-i\alpha} \tag{33}$$

- Doublet:
$$W(z)_{doublet} = -\frac{u_0 \, r \, 2 \, e^{-i\alpha}}{(z - z_c)^2} \tag{34}$$

- Vortex:
$$W(z)_{vortex} = \frac{-i \, \Gamma}{2\pi \, (z - z_c)} \tag{35}$$

Again, by applying the superposition principle, the total complex velocity is obtained:

$$W(z)_{cylinder} = W(z)_{uniform} + W(z)_{doublet} + W(z)_{vortex} \tag{36}$$

Finally, the potential velocity field is given by:

$$u = Re(W(z)_{cylinder}) \tag{37}$$

$$v = -Im(W(z)_{cylinder}) \tag{38}$$

The remaining aerodynamic parameters may be obtained by considering an isentropic-isoenergetic flow field with known upstream values.

4.2   Flow around a Van Der Vooren airfoil

The Van Der Vooren transformation [23] creates a symmetrical airfoil from a circle centered at the origin in the complex plane. This transformation enables changing the airfoil thickness and the trailing edge angle by modifying the thickness parameter "t" and the Karman-Trefftz parameter "K" respectively:

$$Z = 2r + \frac{(z - r)^K}{(z - r \, t)^{K-1}} \tag{39}$$

$$\frac{dZ}{dz} = \frac{K \, (z - r)^K * (z - r \, t)^{1-K}}{z - r} + \frac{(1 - K) \, (z - r)^K \, (z - r \, t)^{1-K}}{z - r \, t} \tag{40}$$

$$K = 2 - \frac{\theta}{\pi} \tag{41}$$

Note that the "Kutta condition" is achieved by imposing a non-zero vortex singularity on the original complex plane [22, 23].

5   Data generation

5.1   Potential flow

The potential flow data is generated in Paraview by an in-house plugin called "Potential Flow Generator" previously developed at ISAE-Supaero. It executes a Python file that creates a structured mesh around the geometry (cylinder or airfoil) and calculates the potential flow parameters based on a user defined input settled on a dedicated GUI.

For the cylinder, a radius of 0.1234m is selected and a domain of height/width = ±125/±20 radius was chosen. An O-type structured mesh of 600 points along the radial direction and 1001 points along the circumferential direction was used, with exponential radial refinement as shown in Fig.2. The upstream reference values are Ps=101325 Pa and Ts=288K and the velocity is varied from 0.01m/s to 100m/s (the latter corresponding to an upstream Mach number of 0.3).
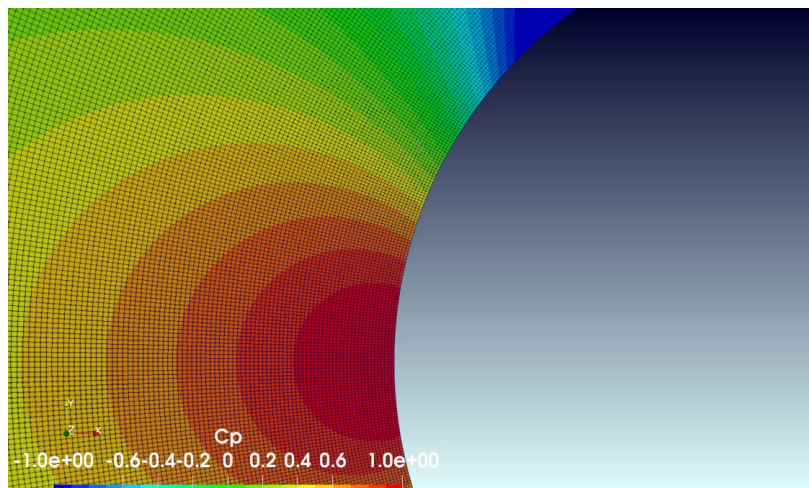
Fig. 2   Grid detail around the leading edge and Cp distribution

The Van Der Vooren airfoil with sharp trailing edge was obtained by transforming the previous cylinder domain. The result is shown in Figures 3 and 4. As a matter of fact, the selected cylinder radius was chosen in order to obtain an airfoil chord of 0.435m after the transformation. The thickness-to-chord ratio is 15% (This was achieved by setting a thickness parameter of 0.06573) and the trailing edge angle is 15°. The resulting domain height is ±62.5m (≈ ±143.4 chords).
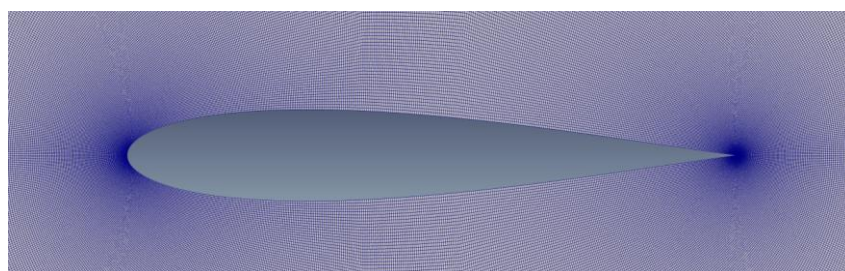
Fig. 3   Van Der Vooren airfoil mesh
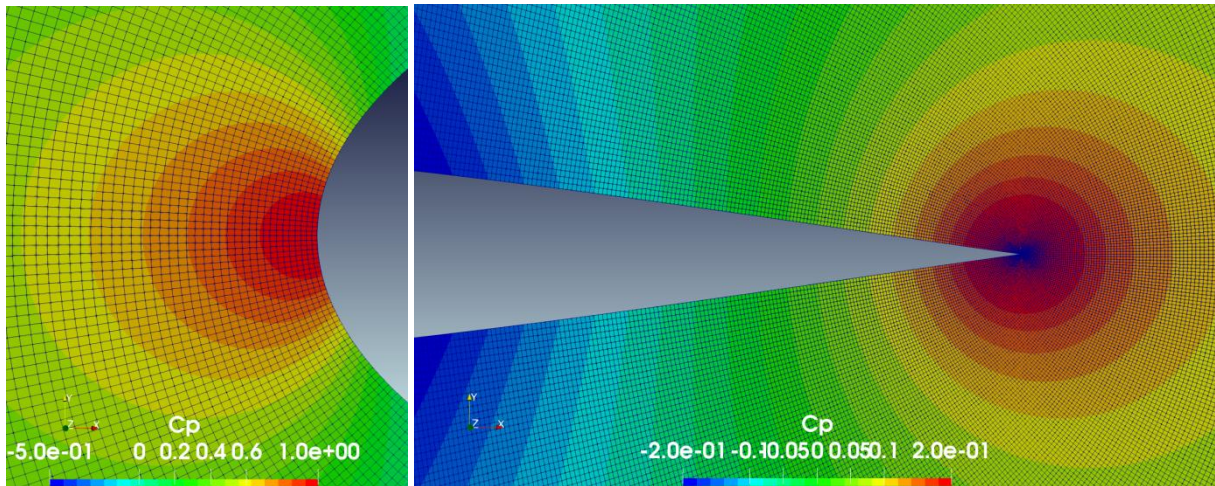
Fig. 4   Grid detail around the leading edge (left) and trailing edge (right) with the Cp field (α=0°)

5.2   CFD RANS/EULER

The airfoil geometry issued from the Van Der Vooren transformation is exported into a CSV file in order to recreate the CAD airfoil geometry in CATIA. Then, a C-block structured grid with wake refinement was created in ICEM CFD (See Fig. 5), with a domain extent of 150 chords in all directions. Since no experimental data is available for this airfoil, a grid convergence study is performed as shown in Fig.6.
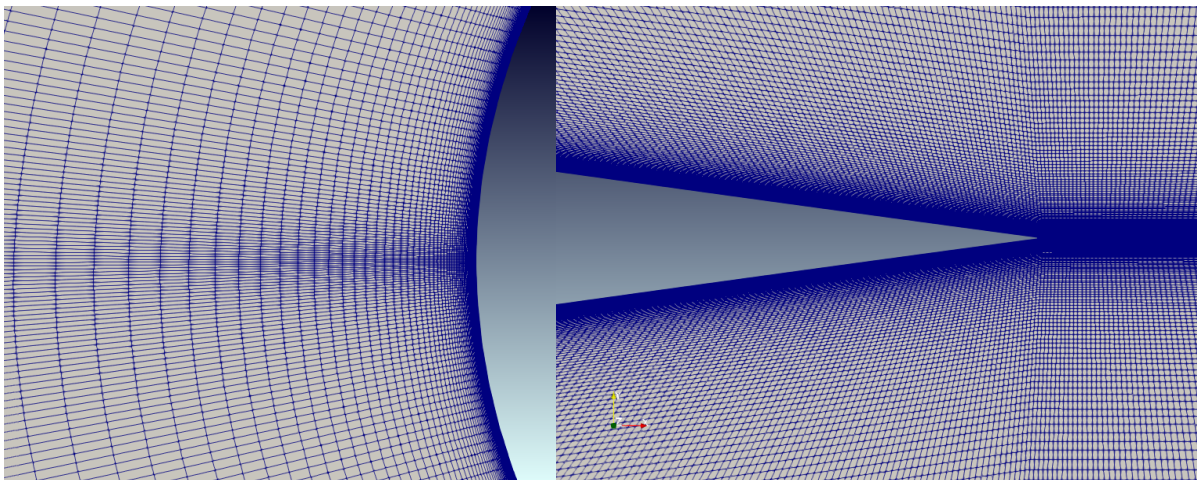
Fig. 5   Grid detail around the leading edge (left) and trailing edge (right) for α=0°

The RANS and EULER solutions are computed with ANSYS Fluent CFD software for several angles of attack at a constant Mach number of 0.3 and a Reynolds number of $3x10^6$. The RANS simulations are performed with the Spalart Allmaras turbulence model. A first quick convergence was done with a first-order discretization (flow and turbulence) by about 3000 iterations, followed by a final second-order discretization convergence as shown in Fig. 7. All the simulations were left running until the near-field drag coefficient residual varied less than 0.1 drag counts from one iteration to the following. At the same time, the residuals must be stabilized at their maximum precision in order to ensure that the airfoil's losses were completely transmitted (convected) downstream. Then, the y^+ parameter is controlled in order to verify that $y^+ \leq 1$ everywhere around the body as required by the Spalart Allmaras model (Fig. 7).
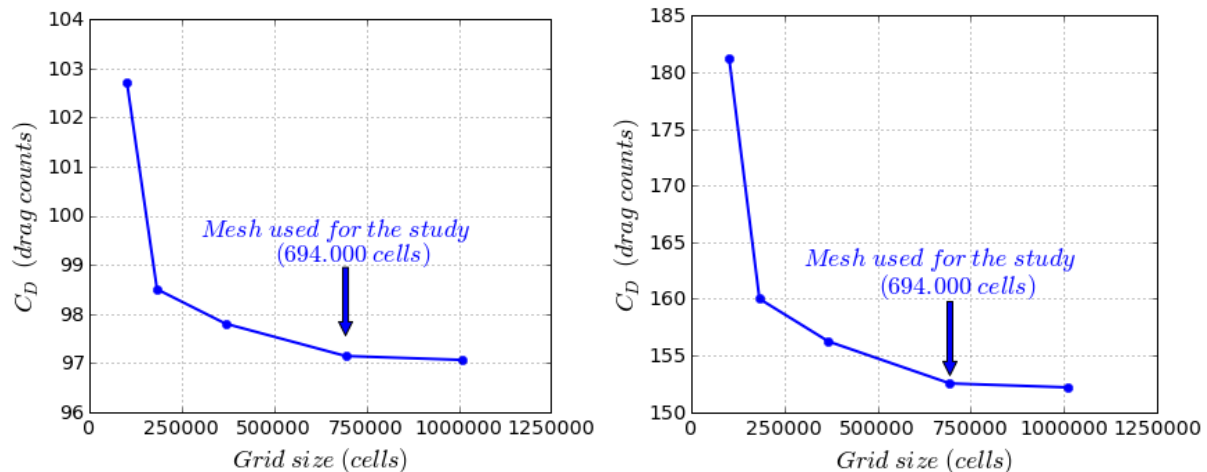
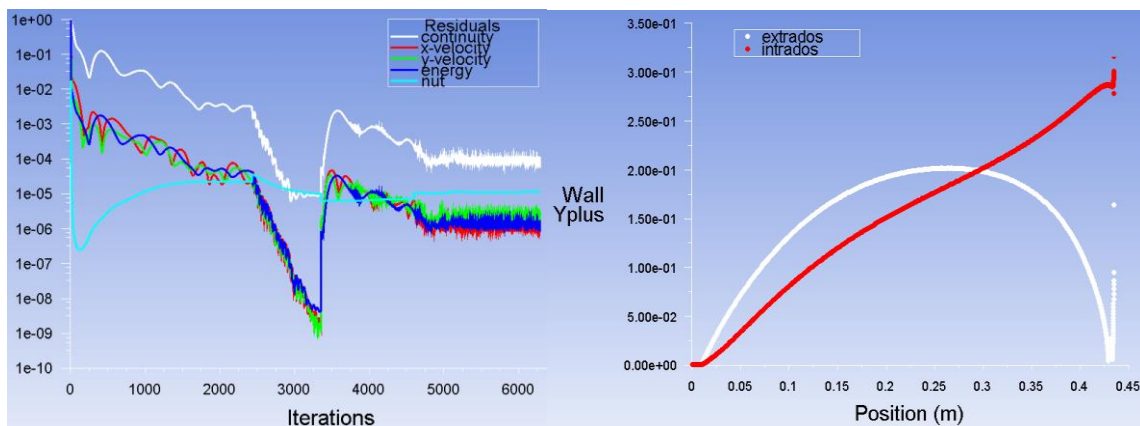*Fig. 6   Grid convergence for α=0° (left) and α=10° (right) at M=0.3 and Re=3x10^6*

Fig. 7   Residuals convergence (left) and y$^+$ distribution (right) for the airfoil at α=10°/M=0.3

5.3   Posttreatment

The data was analyzed with a Paraview's plugin called Epsilon, which was previously developed by ISAE-Supaero. It consists of several python files loaded into Paraview enabling the calculation of the far-field and exergetic parameters based on the CFD or potential flow data.

6   Potential flow analysis

The 2D potential flow around a cylinder is studied first. The case study is a cylinder submerged in a uniform flow of 10 m/s (The velocity is limited to 10 m/s –corresponding to a freestream Mach number of M=0.03- in order to avoid the compressibility effects).

The mechanical exergy, thermal exergy and the drag coefficient fields are shown in Fig. 8. Moreover, its related distributions are displayed along a black survey line placed at 0.5 radius downstream of the body and perpendicular to the upstream direction. Note that the potential flow is inviscid, thus isentropic: there is no entropy creation in the domain. Hence, the anergy field is zero everywhere (that's why it is not displayed). As a reminder, the drag coefficient field is the addition of the mechanical, thermal and anergy fields.

The mechanical exergy field has positive and negative regions as it was explained in [12], however the integral of this field along the survey line gives a negligible negative value (less than 0.1 power counts in magnitude). On the other hand, the thermal exergy field is always positive as it was demonstrated by Arntz [9], thus, its integral along the survey line gives a very small positive number. The key point here is that the integrals of the mechanical and thermal exergies in a potential flow are always equal in magnitude but opposite in sign: the thermal exergy is positive and the mechanical exergy negative. As a consequence, the integral of the drag coefficient along the survey line is strictly zero. This result was expected because it is well known that the drag of a body in a potential flow is zero [15]. Another interesting feature is that the magnitude of the thermal exergy local values are several orders of magnitude smaller than the local values of the mechanical exergy (that's why the C_D and E_m fields are quite similar), however, their integrals are of the same magnitude.
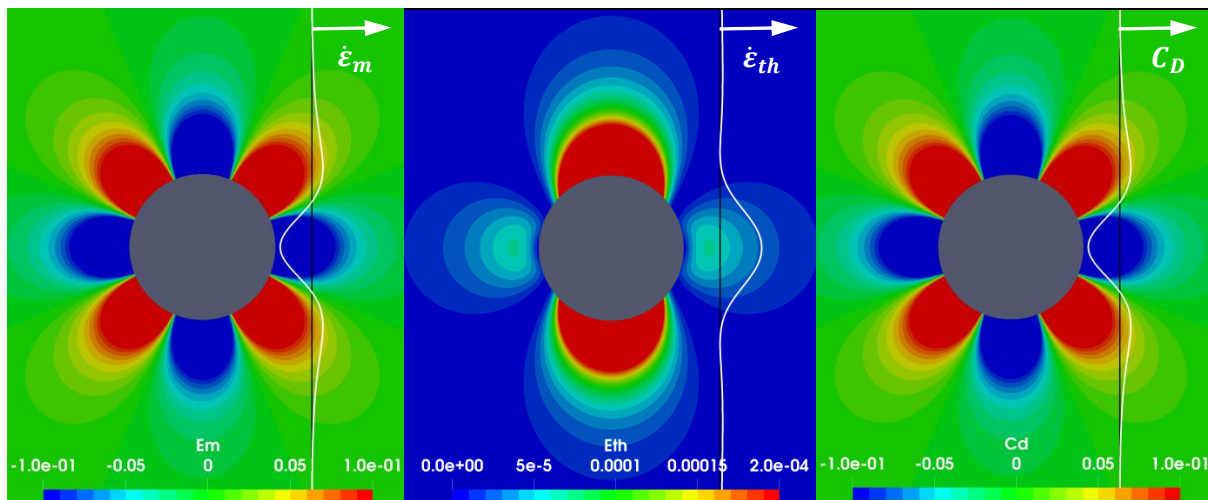
Fig. 8 Mechanical exergy (left), thermal exergy (center) and drag coefficient (right) fields

The exergy concept states that any perturbation of the system (perturbation of speed, pressure, temperature) has an inherent energetic potential: the system can be returned to its original (equilibrium) state by means of a reversible transformation, enabling the extraction of some work from the field. Thus, at a first glance, the thermal and mechanical fields are allegedly recoverable even in a potential field case. However, it must be noticed that any streamline follows an isentropic path and that the perturbations suffered by a fluid particle are reversible all along this path. Hence, the net work done by a small volume of fluid is zero at the end of the process. There is no work potential available downstream of the body, even though the mechanical and thermal components are non-zero (because they are equal and opposite quantities). The key point here is that in a potential flow no exergy recovery is possible: the exergy related to the potential perturbations is self-recovered because of the reversible process followed by the fluid. This result is still valid even in the case of the cylinder with circulation (not shown here).

The next step is to apply a Van Der Vooren transformation to the cylinder in order to obtain the potential flow past an airfoil as shown in Fig. 9. Since the C_D and E_m fields are almost identical (as it was explained before), only the mechanical and thermal fields are displayed. Moreover, a black survey line is placed 1% chord downstream of the trailing edge and the distribution of the field is displayed along this line. It can be seen that the transformed field conserves the same distribution pattern as it was observed for the case of the cylinder but somewhat distorted because of the conformal mapping. Again, the net mechanical exergy available in this potential flows is zero, even though it may be non-zero locally. Also, the thermal and mechanical exergies integrals are equals and opposite in sign as

before. This means that the results found for the cylinder are still valid for an airfoil even in a lifting condition (not shown here).
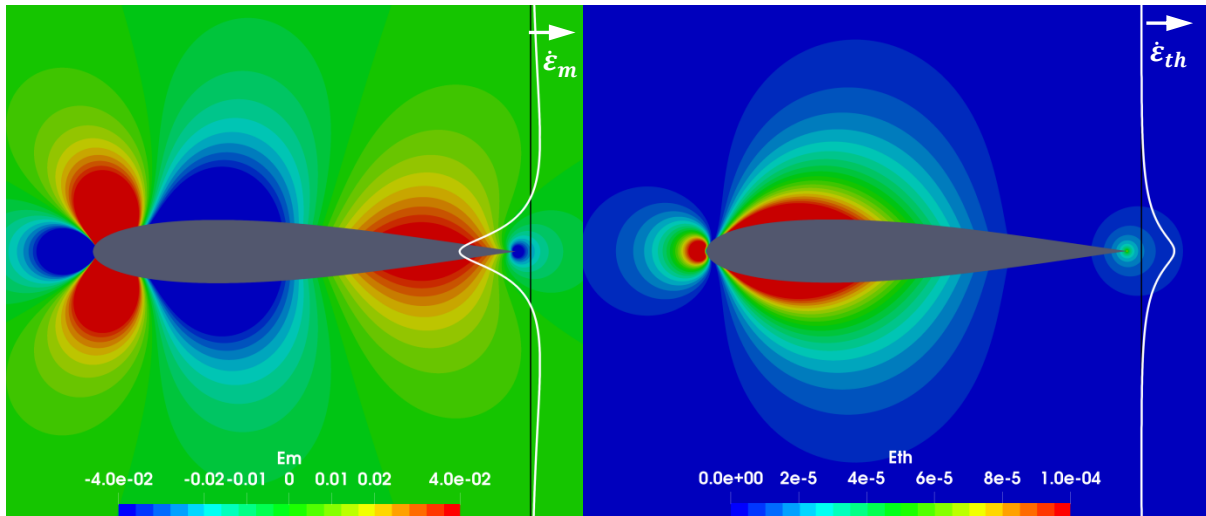

Fig. 9   Mechanical exergy (left) and thermal exergy (right) fields

7   Compressibility analysis

The flow around a cylinder shown before corresponds to a low-speed condition (10 m/s). The effect of increasing the speed is shown in Fig. 10. It can be seen that the thermal and mechanical exergy integrals are no longer negligible but they are still opposite in sign (with the thermal exergy always positive). The drag coefficient is still zero as expected, thus it can be said that the mechanical and thermal exergies are always coupled in a potential flow in such a way that the resulting C_D is always zero.
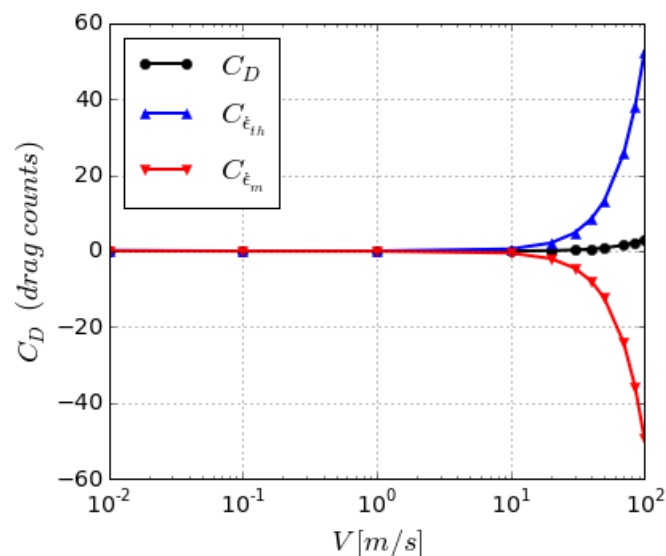
Fig. 10 Evolution of the exergy parameters with the speed (Potential flow – cylinder)

Since the potential flow past a cylinder is symmetrical, this graphic is identical for a survey line placed at the same distance from the body upstream or downstream. However, if the survey line is placed farther from the body, the magnitude of the thermal and mechanical exergy integrals starts being

reduced. Also, note that some numerical errors start being noticeable as the speed increases: the C_D values are not strictly zero. This is because the potential flow code considers a constant density (that's not true as the speed increases).

In order to avoid the calculation errors related to the potential flow at relatively high-speed, an EULER solution of the Van Der Vooren airfoil at zero angle of attack was performed. The related integrals are shown in Fig. 11 for two survey planes placed 1% chord away from the leading edge and the trailing edge respectively. The same result found for the cylinder is obtained here again for the airfoil. Note that this time the EULER solution provides a zero C_D value for the high speed condition as expected. Also note that the magnitude of the integrals is smaller for the survey plane placed at the trailing edge. This is because the mechanical and thermal fields are no longer symmetrical respect to the Z-axis (as it was the case for the cylinder) but somewhat attenuated at the trailing edge because of the smaller perturbations created by the airfoil in that region.
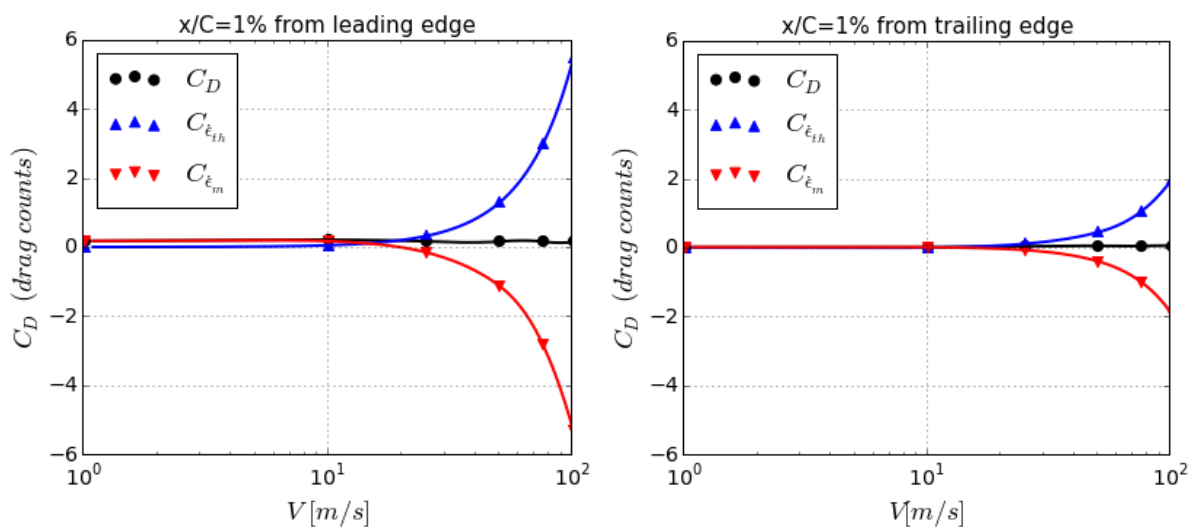

Fig. 11 Evolution of the exergy parameters with the speed (EULER / Van Der Vooren airfoil / α=0°)

8   Viscous flow analysis

The final step of the analysis is to add the viscous effect to the flow field by using a RANS CFD solution. Figures 12 and 13 show the RANS flow around a Van Der Vooren airfoil for an angle of attack of 10°. In those figures, a black survey plane is shown placed at 1% chord downstream of the airfoil as well as the field distribution along this survey line. This time, the anergy field is no longer zero and the C_D field is built up by summing up both exergy fields as well as the anergy field.

When the survey line is placed upstream of the body, the same results as the EULER solutions are obtained: the drag coefficient integral is zero and the mechanical exergy integral is equal and opposite to the thermal exergy integral. However, when the survey planes are placed downstream of the body (as shown in Fig. 13) this is no longer true: there is a net positive drag coefficient and the integrals of the mechanical and thermal exergies are no longer equal and opposite. This is clearly a consequence of the viscosity. As a matter of fact, the fluid particles that enter into the boundary layer or the wake follow a non-isentropic path and the perturbations suffered by a fluid particle are no longer reversible. Thus, there is a net work available downstream of the body, reflected as a drag.

The fact that the particle follows a non-isentropic path is depicted by the increase of entropy (anergy creation). Moreover, by following a non-isentropic path during the process (i.e., during the perturbations suffered along the streamline), there will be a net work available in the particle as

reflected by the increase of exergy in the viscous zone. According to the exergy principle, this exergy is recoverable. However it must be realized that not all this exergy is recoverable because the viscous field is built up on the top of a potential flow field base. The exergy related to this potential flow field base is self-recovered as it was demonstrated before. Thus, only the viscous part is potentially recoverable.
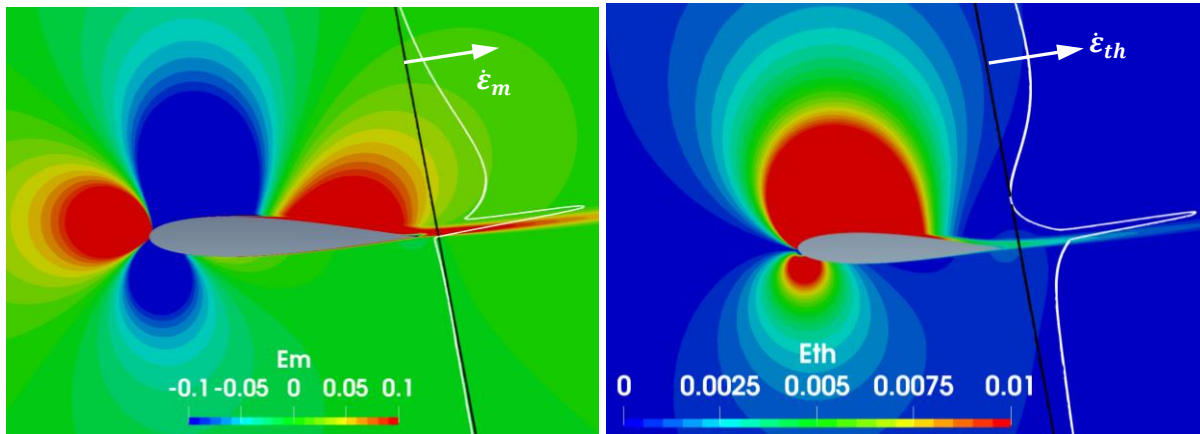

Fig. 12 Mechanical exergy field (left) and thermal exergy field (right) for α=10° and V=102m/s
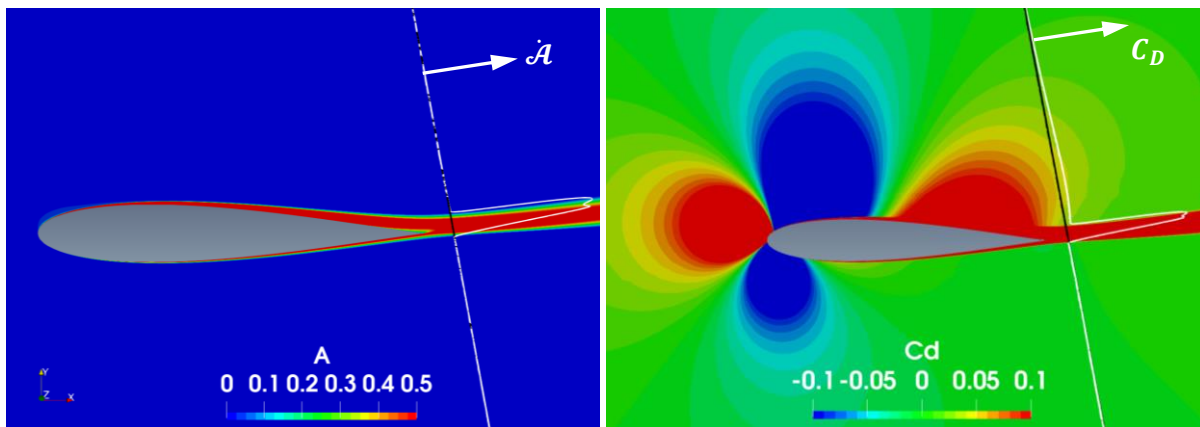
Fig. 13 Anergy field (left) and drag coefficient field (right) for α=10° and V=102m/s

In order to further investigate this aspect, the exergy breakdown technique is used. This allows decomposing a RANS CFD field into its viscous and isentropic fields as shown in Fig.14 for the drag coefficient field (this decomposition is also realizable for the thermal and mechanical fields, not shown here).

Then, a survey plane is placed downstream of the body and the drag coefficient distribution is plotted along this line for the 3 fields: RANS (violet), isentropic (white) and viscous (cyan), as shown in Fig. 15. A close up of those distributions is displayed in Fig. 16.

It can be seen that the viscous profile is zero outside the wake as expected. Moreover, the isentropic profile joins both extremes of the wake by following a potential-like C_D profile. This is the basis of the exergy-breakdown method [21].
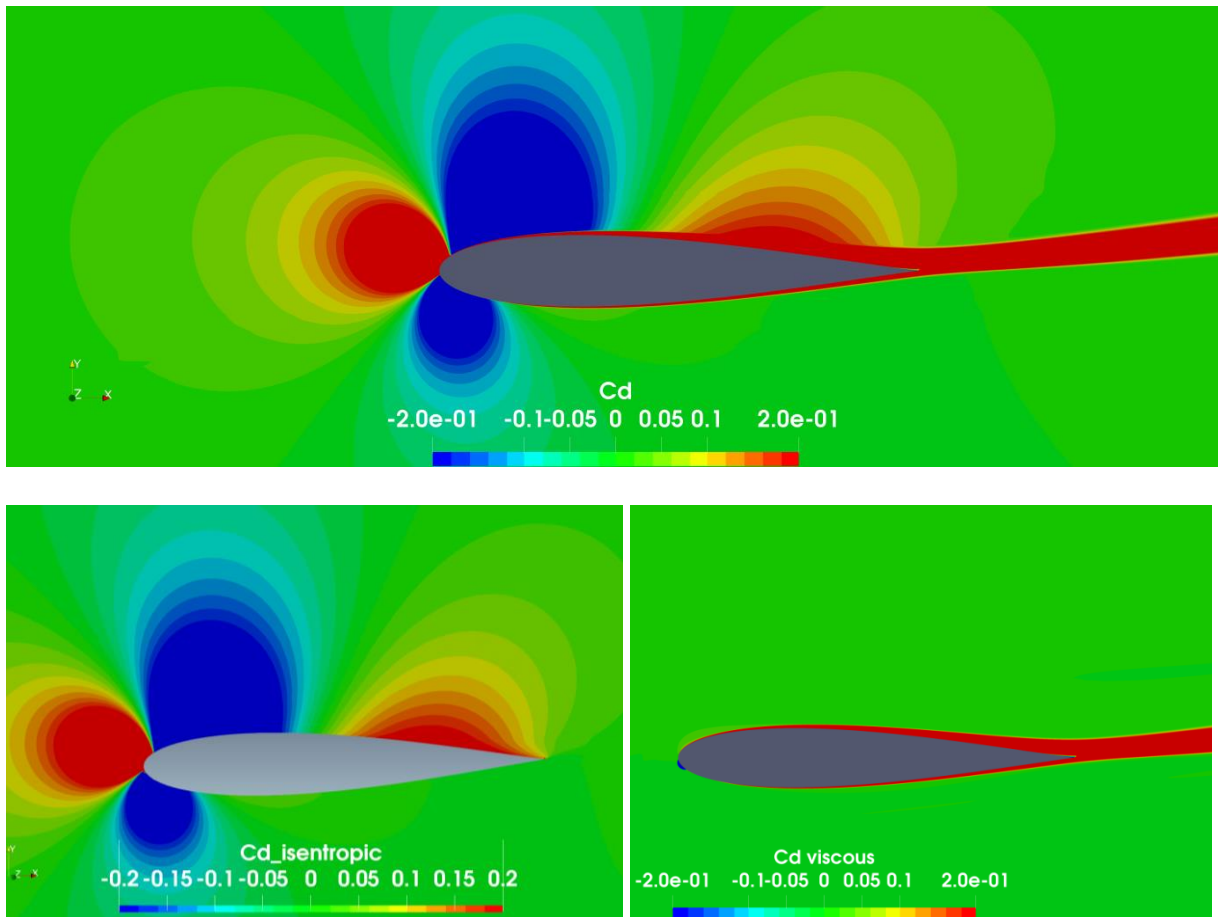
Figure 14: RANS solution (up), isentropic field (left) and viscous field (right) for α=10° and V=102m/s
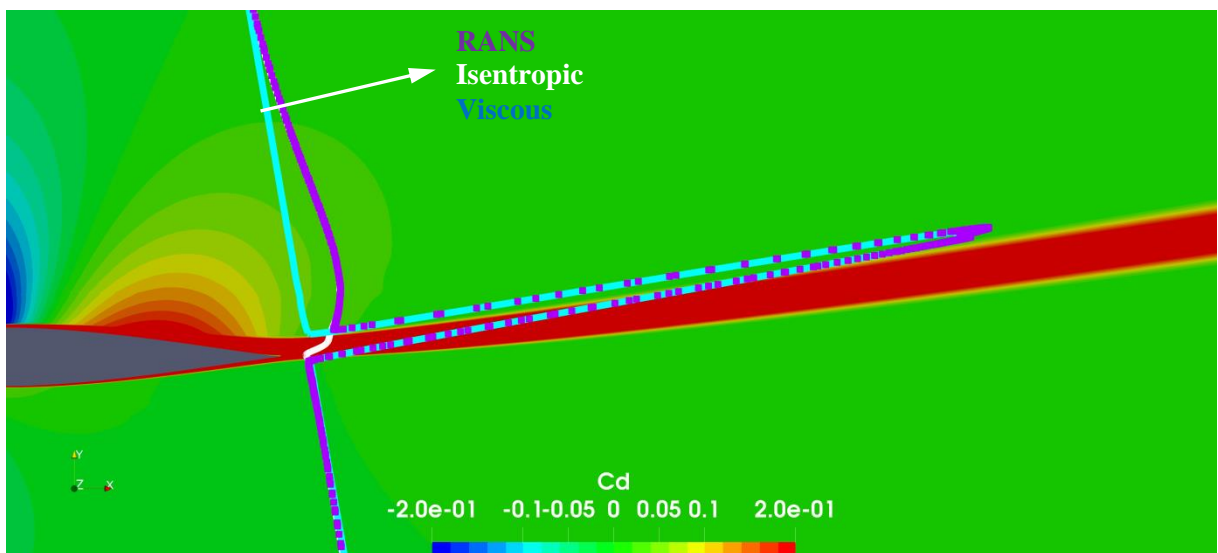

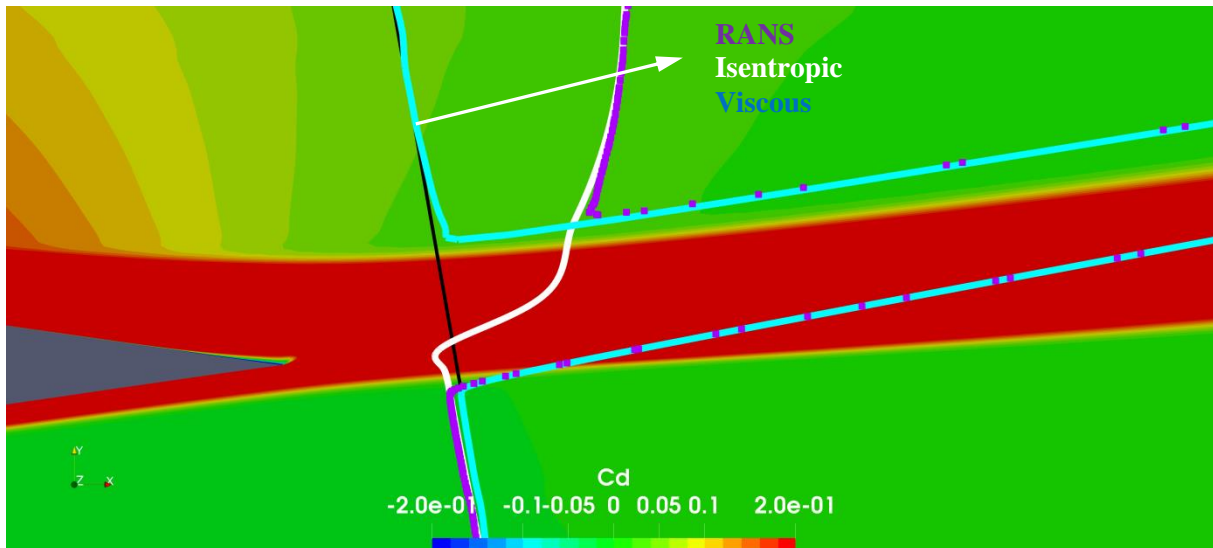*Figure 15: drag coefficient components distribution along the survey line*

Figure 16: close up of the drag coefficient components distribution at the trailing edge area

However, when this isentropic C_D profile is compared against the EULER C_D profile for the same angle of attack, some differences become evident as shown in Fig. 17 (white line for the isentropic C_D and red line for the EULER C_D). This is because the viscous effect changes the effective geometry of the airfoil [14], reducing its lift coefficient (C_L =1.12 for RANS and C_L =1.29 for EULER). This change in lift coefficient creates a change in the flow field and the resulting distributions are no longer comparable. Thus a fair comparison between the EULER and isentropic RANS C_D profiles should be made at constant lift coefficient. That's why on the same figure an EULER solution C_D profile was added, corresponding to an angle of attack of 8.5° (whose lift coefficient is C_L=1.09). Now the isentropic C_D profile from the RANS solution approaches the EULER C_D profile everywhere but inside the wake.
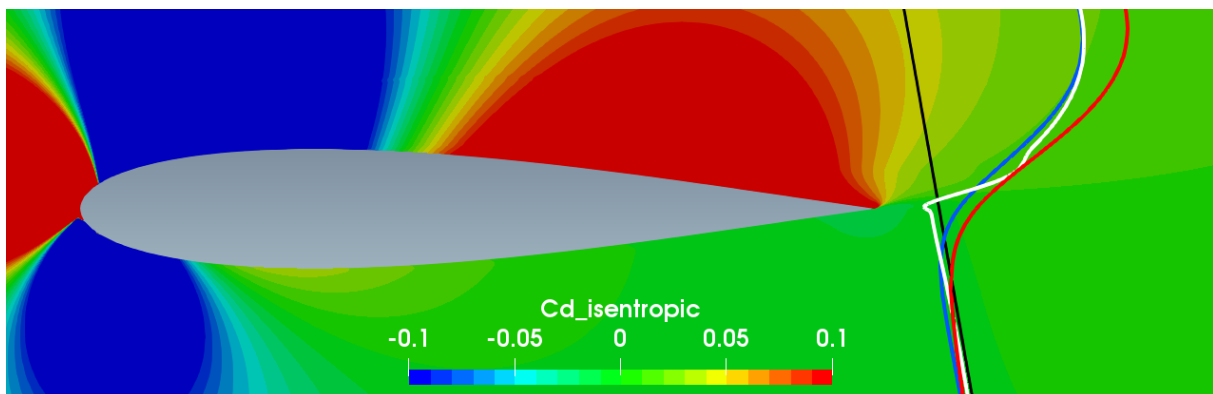

Figure 17: Cd plot for RANS α=10° (white), EULER α=10° (red) and EULER α=8.5° (blue)

For the EULER solution, the C_D profile integral along the survey line is zero, but for the RANS solution the integral of the isentropic C_D profile is not zero. Instead, there is a significant amount of drag counts as shown in Fig. 18 for zero angle of attack (the curve behaves in a similar fashion for other angles of attack).
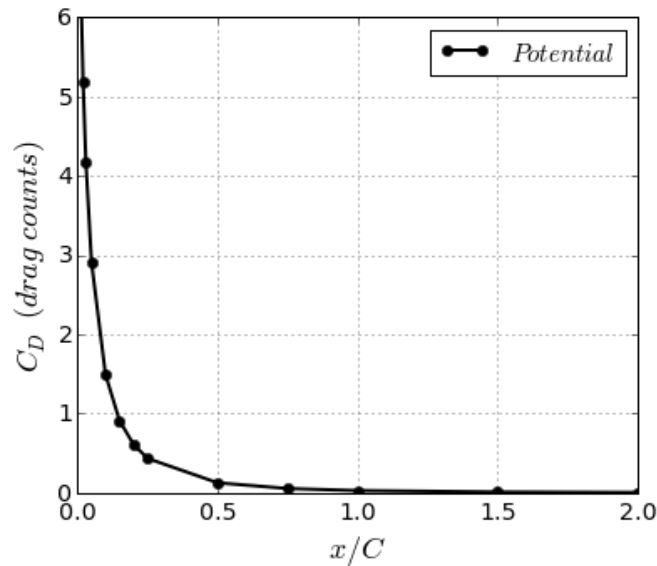
Figure 18: isentropic drag evolution with the survey plane position downstream of the airfoil at α=0°

This means that the isentropic field extracted from the RANS CFD solution is not strictly equivalent to a pure potential or EULER field. Instead, this isentropic field contains a trace of the interaction between the viscous zone (boundary layer /wake) and the rest of the field. Hence, this interaction is a source of drag, and this explains why the integral of the isentropic C_D field is not zero. Even more important is the fact that this integral value increases as the survey plane moves closer to be body. Its value only becomes negligible when the survey plane is at least at one chord downstream from the trailing edge (where the potential C_D field also becomes negligible). This finding will be exploited in the next section in order to propose an improved exergy-based drag prediction method.

6   A new exergetic drag prediction method

Before introducing the new formulation, a review of the existing drag prediction methods will be made as shown in Fig. 19, where some formulations are evaluated for several survey plane positions (for α=0°). The near-field drag value curve is used as a reference to evaluate the performance of the other methods. First, a complete survey plane is considered and the Arntz method implemented. For this case, a very good correlation with the near-field value is observed for any survey plane position. However, it is reminded here that the Arntz formulation is only adapted for CFD simulations but not for wind tunnel testing. In an experimental setup, ideally only the wake data should be surveyed. Thus, hereafter the survey plane size is reduced to the wake. In this condition, the Arntz method, the exergy-breakdown method ("Viscous drag") and the Meheut method performs well for survey planes farther than 1 chord. However, all of them strongly under predict the reference drag value when the survey plane gets closer to the body. This is because the survey plane enters into the viscous-isentropic interaction region of a body as explained before in Fig. 18: its associated drag is not taken into account by any of these formulations. Thus a correction is needed.
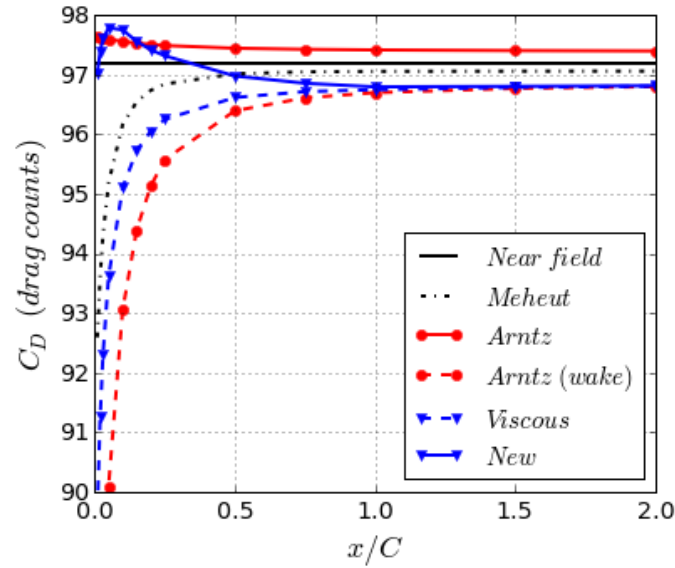
Figure 19: Comparison of drag coefficient values extracted by several methods (α=0°)

In order to do so, the drag associated to the viscous-isentropic interaction must be added to the pure viscous formulations. Nevertheless, the isentropic drag value presented in Fig.18 was obtained from a complete survey plane but in a wind tunnel testing only data inside the wake is available. However, as it was shown before in Fig. 17, the isentropic C_D distribution differs from the EULER C_D distribution mainly inside the wake region. Thus, a good approximation of the infinite integral can be made by only integrating the data inside the wake as shown in Fig. 20. Although its wake integral is negative, its absolute value approximates very well the infinite line integral. Based on this observation, the existing exergy-breakdown formulation can be reformulated as follows:
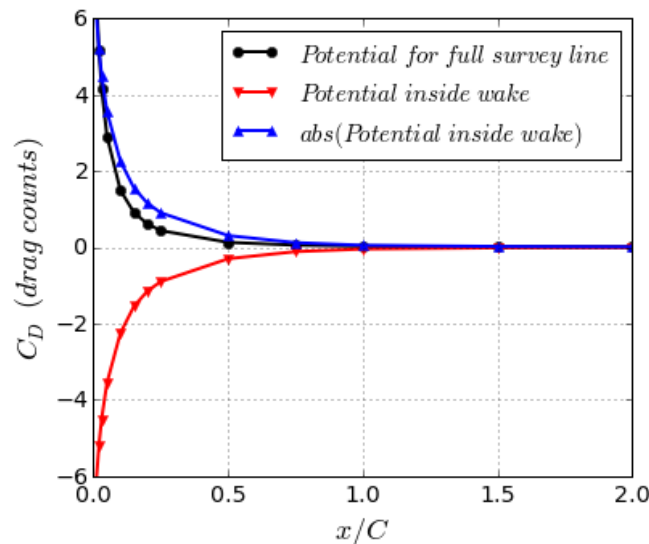

Figure 20: Comparison of the isentropic drag for two different survey line sizes

$$\dot{\varepsilon}_{m_{corrected}} = \int_{S_w} (\overline{\dot{\varepsilon}_{m}} + |\dot{\varepsilon}_{m}^*|_{wake}) dS \tag{42}$$

$$\dot{\varepsilon}_{th_{corrected}} = \int_{S_w} (\overline{\dot{\varepsilon}_{th}} + |\dot{\varepsilon}_{th}^*|_{wake}) dS \tag{43}$$

$$C_{D_{\varepsilon_{corrected}}} = \int_{S_w} \left(\overline{C_{D_\varepsilon}} + \left| C_{D\,\varepsilon}^* \right|_{wake} \right) dS \qquad (44)$$

The corrected C_D value for α=0° is actually plotted in Fig.19 ("new" method curve), where a significant improvement compared to the other wake formulations is observed for survey planes very close to the body. When the angle of attack increases, this correlation gets even better as shown in Fig. 21 for α=10°: the classical uncorrected wake methods are outperformed by the new corrected method even for survey planes extremely close to the body (1% of the chord). This is a big asset of the method because it allows measuring the drag very close to the body as well as the related mechanical and thermal exergies. At that survey plane position, those exergies are maximum and the energy recovery possibilities are also maximum. Hence the interest of improving the existing drag prediction methods.
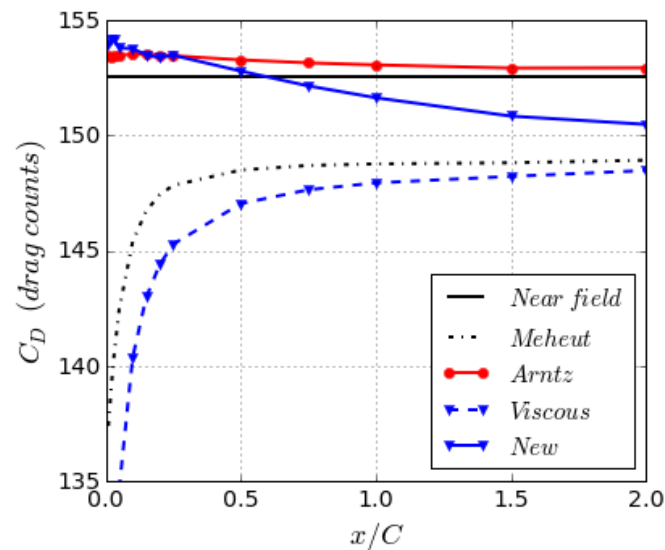

Figure 21: Comparison of drag coefficient values extracted by several methods (α=10°)

Finally, an angle of attack sweep is performed by keeping the wake survey plane fixed at 1% of the chord as shown in Fig. 22, where all the drag methods are compared. The near-field value is kept again as a reference. Moreover, the Meheut method was included in the figure in order to stress the fact that the classical methods fail to accurately predict drag for such a close survey plane. The Arntz method provides an accurate drag prediction but it requires an infinite survey plane size. However, the new corrected expression for the exergy-based drag provides accurate values for the entire angle of attack range, even though the survey plane has been reduced to the wake region.

In Fig.23, the related exergetic quantities are extracted for the Arntz and the new method. It can be observed that the exergy-based drag and the anergy curves are similar for both methods, but the thermal and mechanical exergy distributions are no longer comparable. This is simple to explain because the thermal exergy is always a positive quantity according to the Arntz formulation. Moreover, this formulation integrates the thermal exergy field along an infinite survey line. Thus, both, the inviscid and viscous components are integrated. However, as it was stated before, the inviscid component (related to the potential flow) is self-recovered because there is always an equal but negative potential mechanical exergy that compensates the thermal exergy. Thus, the integration performed by the Arntz method overestimates the real recoverable thermal exergy. However, the new exergy-breakdown method only keeps the recoverable components (viscous + interaction), and thus, it is more meaningful for design purposes: an exergy recovery device will only recover the net exergy (i.e., the difference between the total exergy and the self-recoverable exergy). The same reasoning also applies for the mechanical exergy, which is underestimated by the Arntz formulation because a large

negative mechanical exergy (related to the compensation of the potential thermal exergy) is taken into account on its integration. Finally, it results that the total recoverable exergy is mainly mechanical as shown in Fig 23 (the thermal being almost negligible). In this sense, the Arntz formulation is misleading because it underestimates the true recoverable mechanical exergy and overestimates the true recoverable thermal exergy (This aspect is still under study and will be presented in detail in a future work). The new formulation sheds new light on the physics understanding, especially in the case of the airfoil because the mechanical exergy is predominant and it is easier to recover it (by using BLI) than the thermal exergy (which theoretically would require a thermal machine to recover the related power).
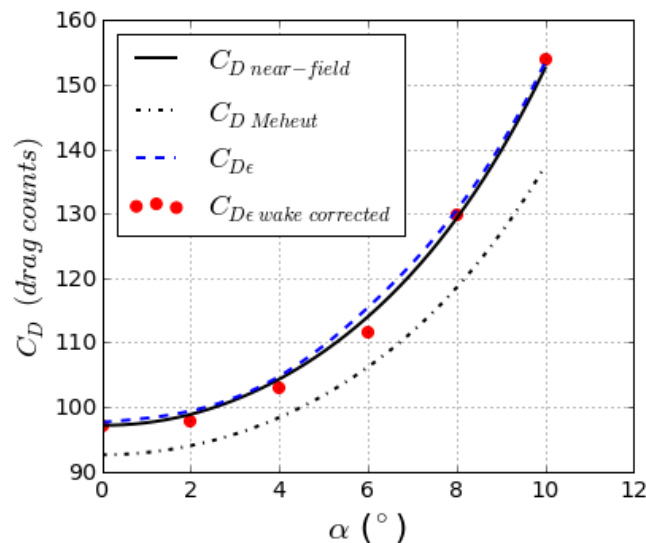

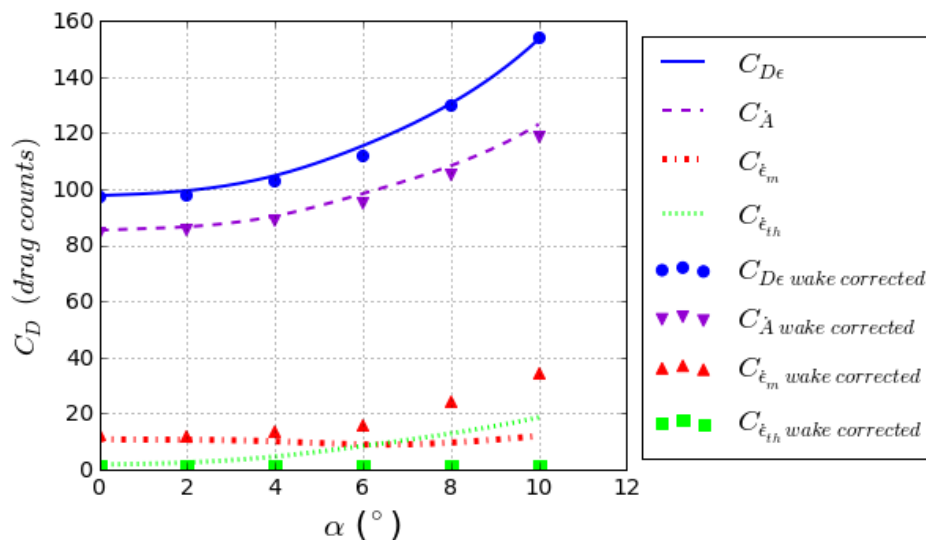*Figure 22: drag coefficient for several methods (survey plane at x/C=1%)*

Figure 23: exergy parameters (survey plane at x/C=1%)

6   Conclusions

The proposed systematic analysis has led to some significant improvement of aerodynamic analyses by using the exergetic method. First, it was found that the exergy-based drag coefficient for a potential

or EULER solution is always zero and that the related thermal and mechanical exergies are equal in magnitude but opposite in sign (a self-compensation of their integrated values). This observation allowed the discovery of a distortion of the isentropic field extracted from a RANS solution due to its interaction with the viscous region and that this interaction zone has associated non-zero drag. This observation led to the proposal of a new exergy-breakdown method well suited for wind tunnel testing with survey planes that are placed extremely close to the body. Moreover, it was demonstrated that the new formulation clearly shows the effective recoverable exergy (mostly of mechanical origin) and, at the same time, takes away the self-recovered part of the exergy.

References

[1] Cengel, Y., Boles, M., Thermodynamics: An Engineering Approach, Eighth edition, Mc Graw Hill Education, New York, 2015.

[2] A.Bejan, Advanced engineering Thermodynamics, Second edition, John Wiley and Sons, New York, 1997.

[3] Paulus, D., Gaggioli, R., "The Exergy of Lift and Aircraft Exergy Flow Diagrams", International Journal of Thermodynamics, Vol.6, (No.4), pp.149-156, December-2003.

[4] Li, H., Stewart, J., Figliola, R., "Exergy Based Design Methodology For Airfoil Shape Optimization And Wing Analysis," 25th International Congress Of The Aeronautical Sciences ICAS, 3rd – 8th September, Germany, 2006.

[5] Alabi, K., Ladeinde, F., Spakovsky, M., Moorhouse, D. and Camberos, J., "The Use Of The 2nd Law As A Potential Design Tool For Aircraft Air Frame Subsystems," International Journal of Thermodynamics, Vol. 9 (No. 4), 2006, pp. 193-205. ISSN 13019724.

[6] D. Riggins, Moorhouse, D., Camberos, J., "Characterization of Aerospace Vehicle Performance and Mission Analysis Using Thermodynamic Availability," Journal of Aircraft, Vol. 47, No. 3, 2010, pp. 904-9016.
https://doi.org/10.2514/1.46420

[7] Camberos, J. and Moorhouse, D., Exergy Analysis and Design Optimization for Aerospace Vehicles and Systems, Progress in Astronautics and Aeronautics, AIAA, 2011. eISBN: 978-1-60086-840-5

[8] Hayes, H., Lone, M., Whidborne, J., Camberos, J. and Coetzee, E., Adopting Exergy Analysis for use in Aerospace, Progress in Aerospace Sciences, Volume 93, pp. 73-94, 2017.
DOI: 10.1016/j.paerosci.2017.07.004

[9] Arntz, A., "Civil Aircraft Aero-thermo-propulsive Performance Assessment by an Exergy Analysis of High-fidelity CFD-RANS Flow Solutions", Fluids mechanics, Université de Lille 1, 2014.

[10] Arntz, A., Altinault, O.," Exergy-Based Performance Assessment of a Blended Wing–Body with Boundary-Layer Ingestion", AIAA journal, Vol. 53, No. 12, December 2015.
DOI: 10.2514/1.J054072

[11] Aguirre, M. and Duplaa, S., "Exergetic Drag Characteristic Curves," AIAA Journal, (Accepted for publication in March 2019).

[12] Aguirre, M., Duplaa, S. and Carbonneau, X., "2D Flow Field Analysis by the Exergetic Method" , AIAA Applied Aerodynamics Conference, 17-21 June 2019, Dallas, Texas, United States.

[13] Aguirre, M., Duplaa, S. and Carbonneau, X., "Vortex Exergy Prediction", 54th 3AF International Conference on Applied Aerodynamics, 25 – 27 March 2019, Paris, France.

[14] Drela, M., Flight Vehicle Aerodynamics, The MIT Press, Cambridge, MA, 2014 ISBN: 9780262526449.

[15] Anderson, J., Fundamentals of Aerodynamics, McGraw-Hill Education, Boston, 2010. ISBN 0073398101, 9780073398105.

[16] Betz, A., "A Method For The Direct Determination of Wing-Section Drag," NACA Technical Report 337, 1925.

[17] Jones, B., "Measurement of Profile Drag by the Pitot-Traverse Method," Aeronautical Research Council R&M Rept. 1688, 1936.

[18] Oswatitsch, K., Gas Dynamics, Academic Press, New York, 1956.

[19] Kusunose, A., "Extension of Wake-Survey Analysis Method to Cover Compressible Flows," Journal Of Aircraft, Vol. 39, No. 6, 2002, pp. 954-963.
https://doi.org/10.2514/2.3048

[20] Meheut, M., "Evaluation des Composantes Phénoménologiques de la Trainée d'un Avion à Partir des Résultats Expérimentaux," Thèse ONERA-Université des Sciences et technologies de Lille, France, 2006.

[21] Aguirre, M., Duplaa, S., Turnbull, A. and Carbonneau, X., "A velocity decomposition method for exergy-based drag prediction," AIAA Journal, (Submitted for publication).

[22] E.Houghton, P.Carpenter, "Aerodynamics for Engineering Students", Fifth Edition, Butterworth-Heinemann, 1993.

[23] J.Katz, A.Plotkin, "Low-Speed Aerodynamics: from wing theory to panel methods", First Edition, McGraw-Hill, 1991.